JACS JOURNAL OF THE AMERICAN CHEMICAL SOCIETY

Article

Cite This: J. Am. Chem. Soc. 2018, 140, 14195−14205

pubs.acs.org/JACS

Reversible and Site-Dependent Proton-Transfer in Zeolites Uncovered at the Single-Molecule Level

Zoran Ristanović,[†] Abhishek Dutta Chowdhury,[†] Rasmus Y. Brogaard,[‡] Klaartje Houben,[§] Marc Baldus,[§] Johan Hofkens,[∥] Maarten B. J. Roeffaers,[⊥] and Bert M. Weckhuysen*[,†]

[†]Inorganic Chemistry and Catalysis, Debye Institute for Nanomaterials Science, Utrecht University, Universiteitsweg 99, 3584 CG Utrecht, The Netherlands

[‡]Department of Chemistry, University of Oslo, Postboks 1126 Blindern, 0318 Oslo, Norway

[§]NMR Research Group, Bijvoet Centre for Biomolecular Research, Utrecht University, Universiteitsweg 99, 3584 CG Utrecht, The Netherlands

[∥]Department of Chemistry, KU Leuven, Celestijnenlaan 200 F, B-3001 Leuven, Belgium

[⊥]Centre for Surface Chemistry and Catalysis, KU Leuven, Kasteelpark Arenberg 23, 3001 Heverlee, Belgium

Supporting Information

ABSTRACT: Zeolite activity and selectivity is often determined by the underlying proton and hydrogen-transfer reaction pathways. For the first time, we use single-molecule fluorescence microscopy to directly follow the real-time behavior of individual styrene-derived carbocationic species formed within zeolite ZSM-5. We find that intermittent fluorescence and remarkable photostability of carbocationic intermediates strongly depend on the local chemical environment imposed by zeolite framework and guest solvent molecules. The carbocationic stability can be additionally altered by changing *para*-substituent on the styrene moiety, as suggested by DFT calculations. Thermodynamically unstable carbocations are more likely to switch between fluorescent (carbocationic) and dark (neutral) states. However, the rate constants of this reversible change can significantly differ among individual carbocations, depending on their exact location in the zeolite framework. The lifetimes of fluorescent states and reversibility of the process can be additionally altered by changing the interaction between dimeric carbocations and solvated Brønsted acid sites in the MFI framework. Advanced multidimensional magic angle spinning solid-state NMR spectroscopy has been employed for the accurate structural elucidation of the reaction products during the zeolite-catalyzed dimerization of styrene in order to corroborate the single-molecule fluorescence microscopy data. This complementary approach of single-molecule fluorescence microscopy, NMR, and DFT collectively indicates that the relative stability of the carbocationic and the neutral states largely depends on the substituent and the local position of the Brønsted acid site within the zeolite framework. As a consequence, new insights into the host−guest chemistry between the zeolite and aromatics, in terms of their surface mobility and reactivity, have been obtained.

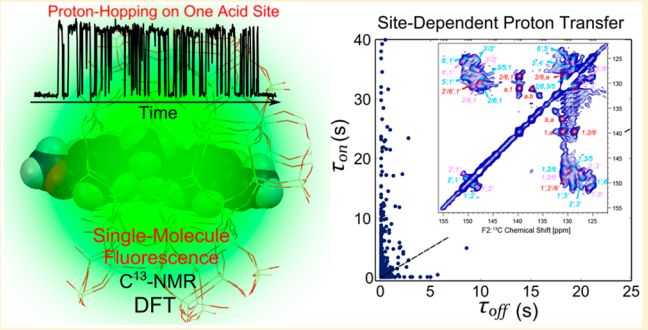

INTRODUCTION

Zeolites are microporous aluminosilicates with tunable acidity and microporous structure that can accommodate and transform numerous organic molecules to valuable chemicals and fuels.[1−3] The Si−O tetrahedra define a highly crystalline and porous matrix that has acidic properties if silicon is substituted with aluminum. A proton transfer and carbocation formation related to the bridging hydroxyl groups in the vicinity of Al, commonly known as Brønsted acid sites (BAS), is of fundamental importance for numerous, large scale acid-catalyzed processes.[4,5] The location of BAS is related to the exact spatial distribution of Al over the available crystallographic sites (known as T-sites).[6,7] In addition to the structural parameters of a zeolite catalyst, the chemical nature of adsorbed reactants, physisorbed intermediates, and solvent environment may significantly affect the proton transfer rates and carbocationic chemistry.[8]

Conventional methods to characterize the chemical nature of acid sites in zeolites include solid-state nuclear magnetic resonance (NMR),[9,10] infrared spectroscopy (IR) based on probe molecules,[11,12] and X-ray absorption spectroscopy (XAS).[13,14] These methods have been used to characterize the heterogeneous population of T-sites in the zeolite framework. Recent advances in atom probe tomography (APT) have opened up new horizons in the sensitive structural characterization of single zeolite particles. This method can be used to map the 3-D distribution of atomic constituents (Si, Al,

Received: July 29, 2018
Published: October 3, 2018

O, and C) before and after a catalytic reaction.[15,16] Nevertheless, it is more difficult to obtain the dynamic picture of organic transformations taking place in zeolite micropores with the ultimate single-molecule sensitivity. For example, industrially important zeolite ZSM-5 contains 12 distinct T-sites that may have nonrandom distribution of Al atoms.[10] There is very little experimental knowledge about the real-time behavior of organic molecules and local proton-transfer processes taking place at individual T-sites. In this respect, single-molecule fluorescence microscopy can provide high spatiotemporal resolution and single-molecule sensitivity.[17−20] In recent years, the technique has provided ensemble-free information about mechanistic single-particle/single-molecule studies of a number of catalytic processes,[21−25] including studies of the related transport phenomena.[26−29] Zeolite catalysis has also benefited from the recent single-molecule fluorescence microscopy studies. By localizing fluorescent products within pores of zeolites, we have elucidated important inter- and intraparticle heterogeneities in acid-catalyzed zeolite chemistry.[30−37] These studies mainly focused on quantitative imaging of single particle reactivity, whereas the potential of single-molecule fluorescence microscopy to disclose intrinsic time-dependent heterogeneities in behavior of individual molecules remained largely unexplored. To the best of our knowledge, this is the first experimental report that studies single-molecule *blinking dynamics* in heterogeneous catalysis, following the ideas from enzymatic single-molecule catalysis[38] and single nanoparticle catalysis.[22,29] It will be shown that it is possible to use fluorescent states of trapped organic species in order to study their real-time interaction with BAS and zeolite framework in an ensemble-free manner.

We have used single-molecule fluorescence microscopy to follow the real-time behavior of carbocationic species confined in the pores of zeolite ZSM-5. To achieve this goal, we employed the Brønsted-acid catalyzed oligomerization of styrene derivatives as a fluorogenic probe reaction.[39−43] Two styrene derivatives, namely 4-methoxystyrene and 4-fluorostyrene, were chosen as probes with different proton affinities (214 kcal/mol vs 200 kcal/mol,[44] respectively) and markedly different proton-transfer rates.[35] Importantly, the probe molecules can fit inside ∼0.5 nm large pores of zeolite ZSM-5, and form highly fluorescent carbocationic species that are additionally stabilized by a tight sterical protection from nucleophilic attacks. Recently, we have shown that by changing the substituent on the styrene moiety, as well as the solvent medium, it is possible to directly study the turnover rates of proton transfer processes with single turnover sensitivity.[35] Here, we take a crucial next step to study real-time dynamics of individual carbocationic species confined in the pores of ZSM-5. As positively charged species, these carbocations are adsorbed in the vicinity of Al atoms and can be used as real-time reporters of interactions between Brønsted acid sites and guest molecules. However, accurate structural elucidation of such guest molecules is also essential to provide in-depth understanding of the host−guest chemistry between the inorganic zeolite and organic guest molecules. In this context, we corroborated the findings from the single-molecule fluorescence microscopy with a detailed investigation of the reaction mechanism by using advanced magic angle spinning (MAS) solid-state NMR spectroscopy and density functional theory (DFT) calculations. These approaches collectively point toward a large diversity of reaction pathways and proton/hydrogen-transfer dynamics taking place within zeolite ZSM-5 crystals. More specifically, a detailed reaction mechanism, including the identification of several mobile and immobile reaction intermediates, as well as the various reaction products during the zeolite-catalyzed oligomerization of styrene is presented.

RESULTS

Single-Molecule Fluorescence Microscopy. The mechanism of the styrene oligomerization involves the formation of fluorescent dimeric and trimeric carbocations that can be efficiently excited with visible light. The spectral properties of fluorescent species formed have been reported previously,[35,43] and recently addressed in a TD-DFT study.[44] Taking into account the reaction mechanism resolved by solid-state NMR (vide infra), we have hypothesized that the fluorescent zeolite-entrapped linear dimeric carbocations (Figure 1a, right) can

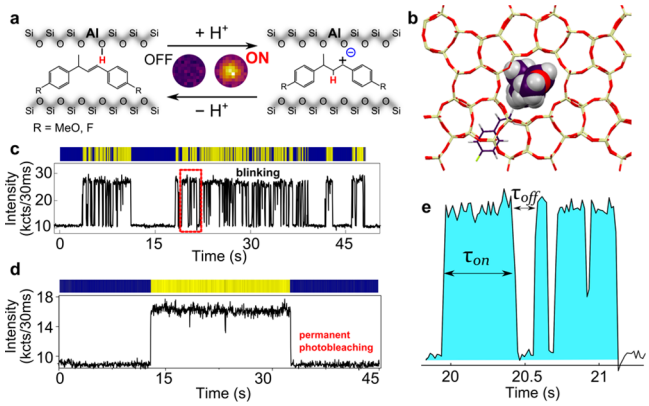

Figure 1. (a) Schematic of the approach to detect protonated, fluorescent dimeric carbocation (bright state on the right); the dark, nonfluorescent state (left) is a neutral dimer that is formed after a proton transfer to the zeolite framework. (b) Representation of the MFI framework (view along *b* axis) and a dimeric carbocation (ball and stick model) trapped along the straight pores; additional monomeric styrene residing in a sinusoidal pore is shown (wire model). (c,d) Blinking (c) and nonblinking (d) fluorescence intensity trajectories of individual carbocationic species of 4-methoxystyrene in heptane. (e) A zoom-in of the trajectory shown in (c), indicating the definition of τ_{on} and τ_{off} times.

transfer a proton to the zeolite framework and yield neutral and nonfluorescent dimeric 1,3-diphenyl-1-butene species (Figure 1a, left). The products are typically formed at the intersections of zeolite ZSM-5 (Figure 1b), leading to a well-defined orientation of fluorescence transition dipole moments along the straight pores of the zeolite.[33,43]

We based our analysis of single-molecule dynamics in zeolites on a statistical description of single-molecule fluorescence intensity trajectories. A wide-field epi-fluorescence microscope was used to simultaneously detect the fluorescent products within ∼25 × 25 μm^2 field of view. In this way, we were able to follow in real time fluorescence intensity of individual emitters, with 30 ms temporal resolution and ∼20 nm localization accuracy.[33] Figure 1 shows an example of two distinctly different fluorescence intensity trajectories. Emitter #1 (Figure 1c) exhibited pronounced blinking, i.e., intermittently present fluorescent and dark states. In contrast, emitter #2 showed constant fluorescence followed by permanent photobleaching (Figure 1d). Careful examination of the scatter plots of individual molecules confirms that the

DOI: 10.1021/jacs.8b08041
J. Am. Chem. Soc. 2018, 140, 14195−14205

observed blinking behavior can be attributed to isolated single molecules (Supporting Information (SI), Figure S1, Supporting Movie S1). We exclude the possibility that the blinking may be explained by the formation or diffusion of new fluorescent molecules, as blinking events were highly localized—i.e., no large single-molecule jumps were recorded within the localization precision of the method (20 nm). Subsequent turnover events happening at one specific acid site are highly unlikely under the conditions of low reactivity, considering also the bulkiness of fluorescent products. As is illustrated in Figure 1a, we initially hypothesize that a single proton-exchange between an individual carbocation and the zeolite framework is possible to be observed by our approach after the dimerization of styrene over zeolitic BAS sites.

We further define the time intervals within the fluorescence intensity trajectories that exhibit alternating fluorescent (protonated, "on") and dark ("off") states, denoted further as τ_{on} and τ_{off} lifetimes, as illustrated in Figure 1e. We only considered "blinking" trajectories (Figure 1c) with at least 5 intermitted fluorescent/dark states; hence, molecules that did not show visible blinking (Figure 1d) were not taken into account with our statistical approach; from now on, we will consider all nonblinking molecules as belonging to one distinct subpopulation of emitters with similar chemical properties.

We have analyzed a total of 110 (4-fluorostyrene) and 60 (4-methoxystyrerene) fluorescence intensity trajectories that exhibited significant blinking behavior. This resulted in more than 1500 pairs of on/off times for 4-fluorostyrene and 3000 pairs for 4-methoxystyrene. The complex nature of individual trajectories is highlighted by typical examples of trajectories recorded for 4-fluorostyrene (Figure 2a) and 4-methoxystyrene carbocations (Figure 2b). The averaged fluorescent $\langle\tau_{on}\rangle$ and dark $\langle\tau_{off}\rangle$ times for all analyzed molecules are presented in Figure 2c. Strikingly, the average lifetimes span 2 orders of magnitude and differ significantly from molecule to molecule. The intensity trajectories of 4-fluorostyrene exhibited strong blinking behavior, with typically <1 s short fluorescent and dark times, $\langle\tau_{on}\rangle = 0.5 \pm 0.7$ s and $\langle\tau_{off}\rangle = 0.7 \pm 1.2$ s), as shown in Figure 2a. Interestingly, the analyzed emitters prefer residing in one of the two states and with slight preference for their dark states, $\langle\tau_{on}\rangle < \langle\tau_{off}\rangle$. In stark contrast, 4-methoxystyrene carbocationic products largely preferred fluorescent states with two times longer average $\langle\tau_{on}\rangle$ times, 2.3 ± 5.7 s, as compared to $\langle\tau_{off}\rangle$ times, 1.1 ± 3.3 s. Additionally, the mean duration of 4-methoxystyrene blinking events was more than 10 times longer (195 s) as compared to 4-fluorostyrene (17 s). Our observations can be explained by the electronic effects of the substituents on the protonated aromatic ring known from electrophilic aromatic substitution. The net effect of the fluoro- group is destabilization, agreeing well with the slight preference toward the dark neutral state. The methoxy- group on the other hand is stabilizing, agreeing with the preference toward the bright cationic state, including some exceptionally photostable emitters that did not show visible blinking.

The averaged τ_{on} and τ_{off} lifetimes do not accurately describe the blinking process as a whole, as fluorescence intensity trajectories consist of multiple alternating states of different and highly dispersed lengths in time. The normalized 2-D histograms of *subsequent* pairs of "on−off" times, i.e., ($\tau_{on(1)}$, $\tau_{off(1)}$), ($\tau_{on(2)}$, $\tau_{off(2)}$), etc., provide more quantitative information about statistical distribution of long and short fluorescent events, and their correlation in time. As expected

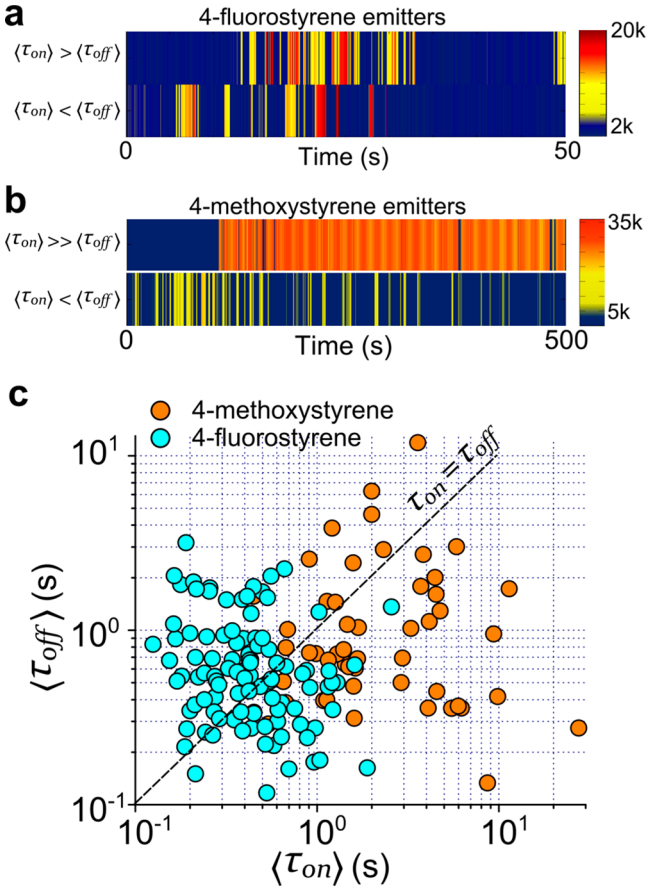

Figure 2. Statistical description of blinking properties for fluorescent products originating from 4-methoxystyrene and 4-fluorostyrene. (a,b) Examples of intermittent fluorescence intensity trajectories for 4-fluorostyrene (a) and 4-methoxystyrene (b), for different ratios of average $\langle\tau_{on}\rangle$ and $\langle\tau_{off}\rangle$ times. (c) Plot of $\langle\tau_{on}\rangle$ and $\langle\tau_{off}\rangle$ lifetimes of fluorescent and dark states for 4-fluorostyrene (blue) and 4-methoxystyrene (red) trajectories. See the SI Figure S2 for cumulative frequency histograms of τ_{on} and τ_{off} lifetimes.

from averaged properties presented in Figure 2c, 4-fluorostyrene predominantly exhibits 100−500 ms long on−off pairs, slightly skewed toward longer "off states" (Figure 3a). This suggests, in average, higher stability of the dark dimeric states of 4-fluorostyrene. The additional autocorrelation analysis of 47 fluorescence intensity trajectories indicated large dispersion of monoexponential correlation times ranging from 0.05 to 1.2 s (SI Figure S3). The large time span indicates diversity of molecular environments that set fluorescent molecules into preferentially bright or dark states (examples shown in Figure 2a).

A normalized 2-D histogram for 4-methoxystyrene shows much broader distribution of "on states" (Figure 3b). The detected fluorescent states span 4 orders of magnitude in measured τ_{on} lifetimes and $\langle\tau_{on}\rangle/\langle\tau_{off}\rangle$ ratios from 0.3 to 100 (SI Figures S2 and S7). Interestingly, we notice two distinct classes of blinking trajectories for 4-methoxystyrene-based carbocations. The first class includes emitters with very long fluorescent states and short dark states. The subsequent (τ_{on}, τ_{off}) pairs of representative 10 molecules of this class with $\langle\tau_{on}\rangle > 5 \times \langle\tau_{off}\rangle$ are collectively plotted in Figure 3c. The (τ_{on}, τ_{off}) pairs of lifetimes are strongly scattered along τ_{on} axis, with $\langle\tau_{on}\rangle = 4.6 \pm 7.9$ s and $\langle\tau_{off}\rangle = 0.5 \pm 0.8$ s. The second class consists of 10 highly blinking emitters presented in Figure 3d. In this

DOI: 10.1021/jacs.8b08041
J. Am. Chem. Soc. 2018, 140, 14195−14205

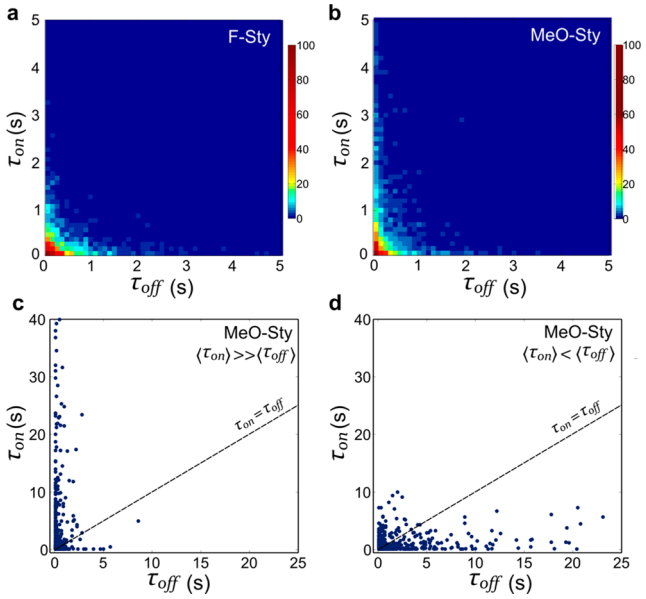

Figure 3. (a,b) Normalized 2-D histograms of all pairs of subsequent τ_{on} and τ_{off} lifetimes collected for 4-fluorostyrene (110 trajectories, 1500 pairs) and 4-methoxystyrene (60 trajectories, 3000 pairs). The histograms are normalized in respect to the (τ_{on}, τ_{off}) pair with the highest occurrence (i.e., 100 ms, 100 ms). The color bars denote the normalized number of detected events for specific (τ_{on}, τ_{off}) values. (c,d) Normalized scatter plots of subsequent (τ_{on}, τ_{off}) pairs of lifetimes for 4-methoxystyrene trajectories categorized based on the average $\langle\tau_{on}\rangle$ and $\langle\tau_{off}\rangle$ times; (c) $\langle\tau_{on}\rangle > 5 \times \langle\tau_{off}\rangle$, and (d) $\langle\tau_{on}\rangle < \langle\tau_{off}\rangle$. Plots in (c) and (d) contain all (τ_{on}, τ_{off}) pairs recorded for 10 trajectories with the specified criteria.

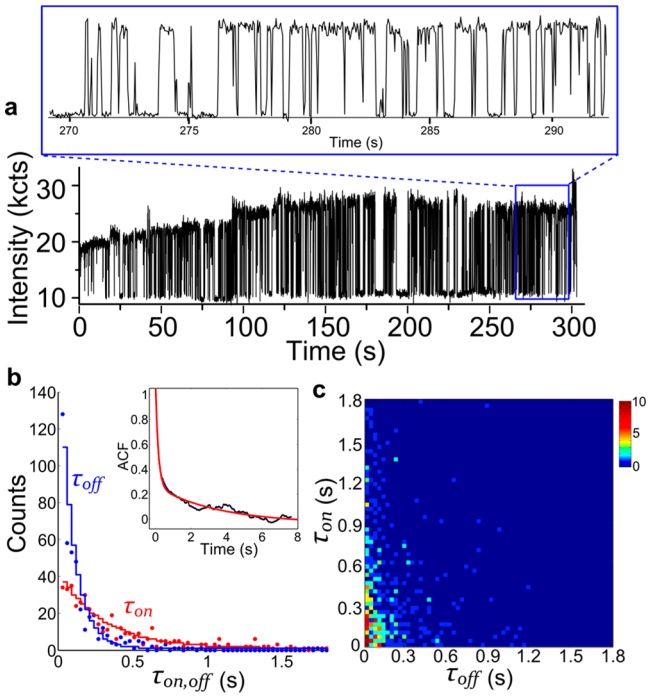

Figure 4. Single-molecule blinking dynamics of the zeolite H-ZSM-5 trapped 4-methoxystyrene-derived emitters in *n*-heptane. (a) Fluorescence intensity trajectory of a highly blinking molecule. (b) Histogram of lifetimes of the fluorescent (red dots) and dark states (blue dots) measured for the single-molecule trajectory shown in (a). Inset: autocorrelation function for the trajectory in (a). Red line is a biexponential fit, with exponential decay constants of $t_1 = 0.16 \pm 0.02$ s (fast-decay component) and $t_2 = 3.6 \pm 0.8$ s (slow-decay component). (c) Real 2-D frequency histogram of the (τ_{on}, τ_{off}) pairs as measured for the trajectory in (a). The color bar denotes the number of detected events for specific (τ_{on}, τ_{off}) values. The simulated 2-D histogram based on the experimentally measured (τ_{on}, τ_{off}) distributions in (b) is shown in SI Figure S4.

case, the dispersion is larger for the dark states ($\langle\tau_{on}\rangle = 1.3 \pm 1.8$ s and $\langle\tau_{off}\rangle = 3.2 \pm 6.7$ s). These two classes encompass at least 40% of analyzed carbocations. Other analyzed trajectories fall in between these two categories, typically with larger fluorescence intervals, $\langle\tau_{on}\rangle > \langle\tau_{off}\rangle$. It should be noted that observed classes of trajectories do not have the expected random distribution of (τ_{on}, τ_{off}) times, but rather highly clustered values of the two parameters are observed. This fact points toward differences among individual emitters that we relate to the carbocation stability at specific T-adsorption sites.

Effect of Solvent Polarity on Blinking Dynamics. The described approach can be generalized and extended to study framework-carbocation interactions in the presence of different guest molecules, such as solvents. Previously, we have shown that the rate constants of 4-methoxystyrene oligomerization can differ dramatically in *n*-heptane and 1-butanol.[35] Fluorescence intensity trajectories of 4-methoxystyrene recorded on parent zeolite crystals in *n*-heptane showed predominantly stable (nonblinking) trajectories with typical lifetimes of 0.1−10 s. However, under the conditions of higher acid site accessibility, such as in steamed zeolites crystals,[35] highly stable and blinking fluorescence intensity trajectories were present. Qualitatively, this behavior was very similar to observed trajectories recorded in solvent-free 4-methoxystyrene (Figure 2). Figure 4 presents fluorescence intensity trajectory and related statistical distribution of τ_{on} and τ_{off} lifetimes for one blinking emitter of 4-methoxystyrene oligomer in *n*-heptane (see also Supporting Movie S2). The average lifetime of fluorescent τ_{on} states was 0.46 ± 0.57 s, approximately 2 times longer than that of dark τ_{off} states 0.23 ± 0.55 s (Figure 4b). The autocorrelation function of the trajectory reveals two processes with different durations (Figure 4b, inset). The fast decay component (0.16 s) corresponds to the large number of short off-states, and the slow decay component (3.6 s) designates a large number of long on-states. Consequently, the distribution of subsequent (τ_{on}, τ_{off}) pairs in their 2-D lifetime histogram is stretched toward longer τ_{on} times (Figure 4c). Interestingly, in the case of 4-methoxystyrene in *n*-heptane, we consistently observe trajectories with $\langle\tau_{on}\rangle > \langle\tau_{off}\rangle$, indicating that carbocationic form of these species is more stable that the neutral (nonfluorescent) state.

An additional experiment in 1-butanol confirms that we are measuring true carbocation-framework interactions. In this case, fluorescence intensity trajectories typically consisted of short <100 ms bursts (Figure 5a). Blinking events were rare, with the distributions of fluorescent and dark states typically the opposite of the ones recorded in *n*-heptane. The histograms of τ_{on} and τ_{off} times are characterized with short fluorescent lifetimes $\langle\tau_{on}\rangle = (0.18 \pm 0.11$ s) and in average 10 times longer dark states $\langle\tau_{off}\rangle = (1.6 \pm 2.2$ s), Figure 5b. Similarly, autocorrelation function of the trajectory has fast decay time of 0.11 s, most likely limited by the acquisition time in our experiments. In this case, the activation energy for the formation of fluorescent carbocations is increased due to solvation of Brønsted acid sites,[35] clearly suggesting that the

DOI: 10.1021/jacs.8b08041
J. Am. Chem. Soc. 2018, 140, 14195−14205

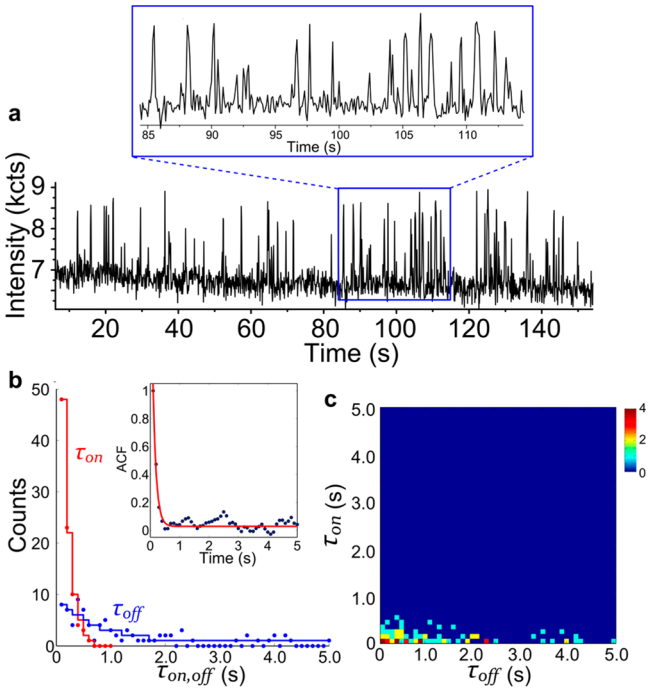

Figure 5. Single-molecule blinking dynamics of the zeolite H-ZSM-5 trapped 4-methoxystyrene-derived emitters in 1-butanol. (a) Fluorescence intensity trajectory of a highly blinking molecule. (b) Histogram of lifetimes of the fluorescent (red dots) and dark states (blue dots) measured for the single-molecule trajectory shown in (a). Inset: autocorrelation function for the trajectory in (a). Red line is a monoexponential fit, with exponential decay constant of $t_1 = 0.11 \pm 0.02$ s. (c) Real 2-D frequency histogram of the (τ_{on}, τ_{off}) pairs as measured for the trajectory in (a). The color bar denotes the number of detected events for specific (τ_{on}, τ_{off}) values. The simulated 2-D histogram based on the experimentally measured (τ_{on}, τ_{off}) distributions in (b) is shown in SI Figure S4.

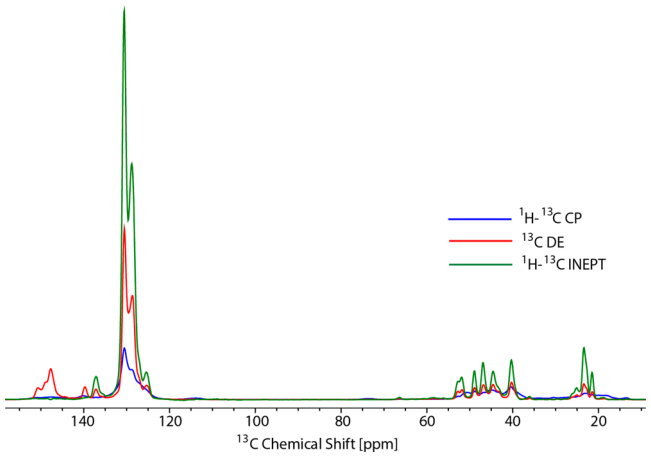

Figure 6. ^{1}H−^{13}C CP (blue, NS = 4096), ^{13}C DE (red, NS = 2048), and ^{1}H−^{13}C INEPT (green, NS = 2048) solid-state NMR spectra (at 15 kHz MAS) of trapped products obtained on H-ZSM-5 after being exposed to $^{13}C_8$-styrene at 393 K (MAS = magic angle spinning, NS = number of scans).

"vicinity of Al-site" is playing an important role in the stabilization of carbocations.

Solid-State Nuclear Magnetic Resonance. With the aim of understanding the mechanism as well as to identify the molecular structures of reaction products of zeolite-catalyzed styrene oligomerization reaction, we employed advanced solid-state NMR spectroscopy on zeolite H-ZSM-5 after being exposed to $^{13}C_8$-styrene. Using of fully isotope-enriched styrene not only significantly increased the NMR signal intensities, but also allowed us to perform multidimensional solid-state NMR correlation experiments to elucidate accurate molecular structures of zeolite-trapped species. The ^{1}H−^{13}C cross-polarization (CP), ^{1}H−^{13}C insensitive nuclei enhanced by polarization transfer (INEPT) and ^{13}C direct excitation (DE) solid-state NMR spectra of the postreacted catalyst are presented in Figure 6. The following three features were primarily observed: (i) 13−52 ppm aliphatic moieties and methyl groups, (ii) 65−75 ppm alkoxy species, and (iii) 112−152 ppm (methylated) aromatic/olefinic groups (Tables S1 and S2). The different solid-state NMR magnetization transfer techniques were previously used for spectral separation of zeolite-trapped species and biomolecules on the basis of mobility.[45−48] As a result, both mobile (i.e., *molecule or group with fast tumbling or rotation*) and rigid (i.e., *molecule physisorbed in/on zeolite*) versions of zeolite-trapped organics have been distinguished in the present case. This spectral separation of mobile and rigid species was envisioned by using through-bond (scalar interactions such as in INEPT)[49] and through-space (dipolar transfer such as in CP)[50] magnetization transfer schemes, respectively. Alternatively, all chemical species, including those that exhibit intermediate dynamics, can be characterized using DE experiments. Comparison of the 1D spectra (Figure 6) shows that the DE spectrum (red) is dominated by mobile zeolite-trapped molecules, as also observed in the INEPT spectrum (green). In addition, linewidths of the rigid molecules (observed in CP, blue) are significantly broader, suggesting heterogeneity in the molecular environment of the physisorbed reactant and product molecules. This observation is consistent with our single-molecule fluorescence results presented in Figure 3.

In the solid-state NMR spectra probing rigid molecules, signals corresponding to the untreated reactant (green lines in Figure 7) are broad or show more than one peak for the same resonance. This can be explained by the same molecule existing in different molecular environments inside the zeolite framework. Interestingly, the signals corresponding to the reactant are absent from the spectra probing the mobile molecules (Figure 6). At least two (solid and dashed green lines in Figure 7) full spin-systems could be identified for the reactant, which we putatively attribute to the (i) "physisorbed state" in zeolite pores by dispersion forces (**A**, Scheme 1) and (ii) the "π-complex" between Brønsted acid sites of zeolites and styrene (**A′**, Scheme 1).[8] In both cases, covalent bonds were neither broken nor formed. This finding actually provides experimental support to a long-standing speculation of multiple adsorption modes of olefin on zeolite, as was recently also emphasized by Lercher et al.[8] The prominent role of a π-complex between zeolitic Brønsted acid-sites and aromatics during zeolite catalyzed hydrocarbon conversion has recently been recognized by us.[48] In addition to the "physisorbed" and "π-complex", we could also identify the zeolite-alkoxy species (**B**, Scheme 1), formed upon adsorption of styrene onto a Brønsted acid site of zeolite (red lines in Figure 7). Also this form of the reactant exists in multiple conformations or molecular environments as doubling or even tripling of the resonance lines is observed. The formation of surface-alkoxy species (**B**, Scheme 1) provides evidence in support of the formation of chemisorbed carbenium species (**A″**, Scheme 1)

DOI: 10.1021/jacs.8b08041
J. Am. Chem. Soc. 2018, 140, 14195−14205

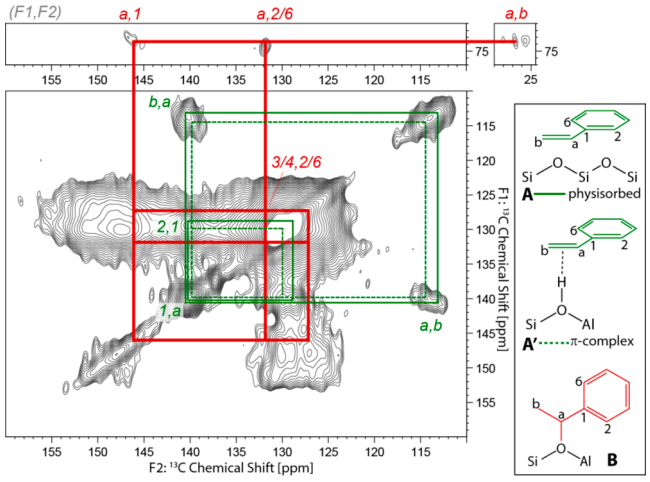

Figure 7. Zooms of 2D MAS solid-state NMR spectra of rigid zeolite trapped molecules. Spectra were recorded on H-ZSM-5 after being exposed to $^{13}C_8$-styrene at 393 K, using 15 kHz MAS. Polarization of the ^{13}C atoms was achieved through cross-polarization (CP) and a 120 ms PARIS[52] mixing period was used. Lines indicate identified spin-systems, in red (surface alkoxide) and in green (styrene), where for the latter at least two forms could be identified as indicated by the solid and dashed lines.

in the process. The identification of **A**−**A**′′ species further supports the influential role of the "vicinity of Al-site" in the stabilization of carbocations during dimerization of styrene reaction, as was also visible from the diverse dynamics of single-molecule fluorescence blinking (Figure 2). Moreover, detection of ethylbenzene ($\mathbf{B_{HT}}$, Scheme 1) can presumably be attributed to the ongoing hydrogen-transfer (HT) side reaction during dimerization of styrene.[51]

Alternatively, products after the reaction, 1,3 diphenyl-1-butene (linear dimeric species **C**, Scheme 1, red spheres Figure 8) and 1-methyl-3-phenylindane (cyclic dimeric species **D**, Scheme 1, in *syn*- and *anti*-stereoisomeric fashion, cyan cross and pink rectangle in Figure 8), were observed in the 2D solid-state NMR spectra using direct excitation, which, as discussed above, for this sample displayed dominantly mobile molecules. Identification of the molecules was achieved, starting from the methyl resonances as observed in panel IV of Figure 8 and concomitant connection to other resonances via the observed cross peaks. For example, an intense cross peak of the methyl resonance at 21.6 ppm (C_d of molecule **D**, Scheme 1) with a resonance at 40.5 ppm (C_c of molecule **D**, Scheme 1) is observed (cyan cross, panel IV Figure 8) and this aliphatic resonance further correlates through a strong peak with 49.0 ppm (C_b of molecule **D**, Scheme 1) and a low intense peak at 52.9 ppm (C_a of molecule **D**, Scheme 1; panel III Figure 8). Further correlations of these aliphatic carbons with aromatic carbons and corresponding intra-aromatic correlations could be identified in panel II and V, respectively. In most cases, correlations with both direct and next neighbors could be identified, as indicated by the solid and dashed lines in Figure 8 panel VI, respectively. As expected, the chemical shifts of the syn- and antistereoisomers of **D** (Scheme 1) significantly differ, for both *magnetically nonequivalent* aliphatic carbons as well as

Scheme 1. Proposed Catalytic Cycle of the ZSM-5 Catalyzed Oligomerization of Styrene Based on Reaction Intermediates and Products Detected in This Study[a]

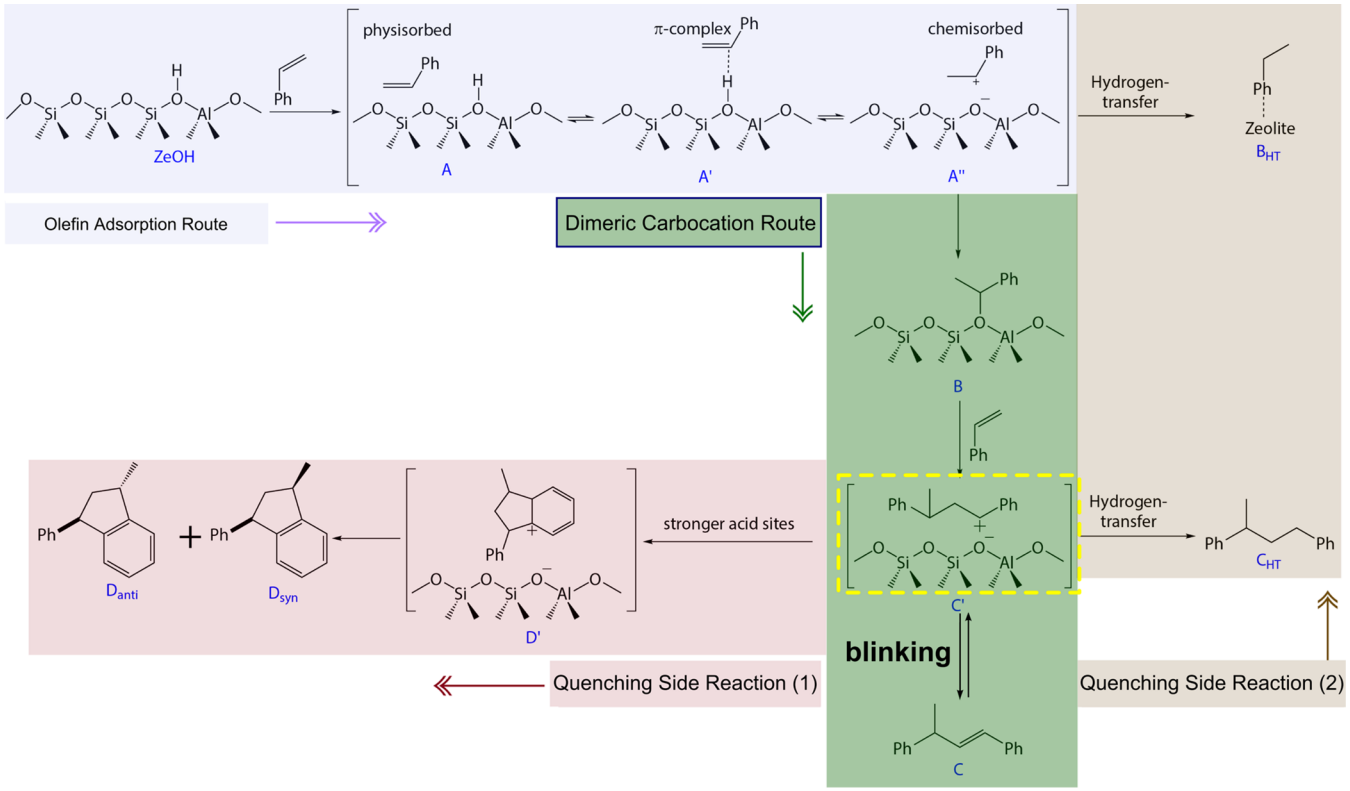

[a]Four distinct adsorption and reaction routes are denoted in different colors. The dimeric carbocation formation route is the most relevant for this study. The dimeric fluorescent species **C**′ are highlighted in the yellow frame.

DOI: 10.1021/jacs.8b08041
J. Am. Chem. Soc. 2018, 140, 14195−14205

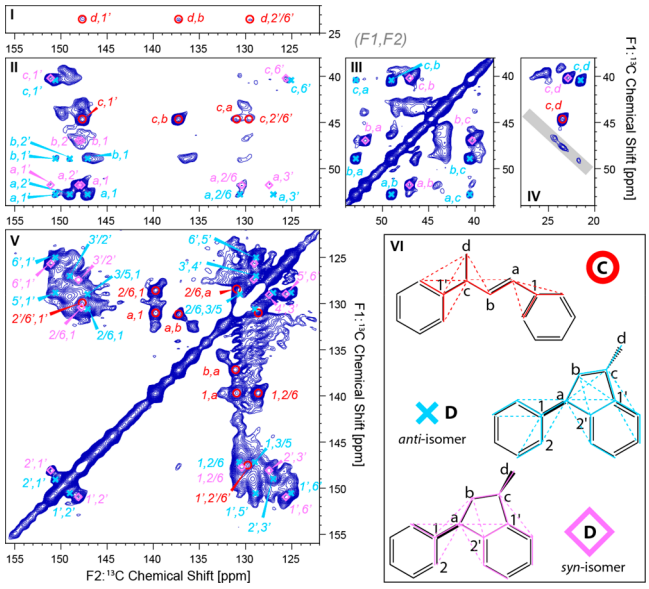

Figure 8. Zooms of 2D MAS solid-state $^{13}C-^{13}C$ correlation NMR spectrum of zeolite trapped products. Spectra were obtained on H-ZSM-5 after being exposed to $^{13}C_8$-styrene at 393 K. ^{13}C atoms were polarized by direct excitation (DE) and a 120 ms PARIS[52] mixing period was used. The MAS frequency was 10 kHz. The gray box in panel IV marks spinning side-bands.

their adjacent aromatic carbons (i.e., C_1, $C_{1'}$ and $C_{2'}$ of molecule **D**). On the basis of the intensities of signals, occurrence of the two stereoisomers is close to equal (cf. ∼47 ± 1% and 53 ± 1% for pink spin-system of *syn*-**D** and cyan spin-system of *anti*-**D**, respectively, based on methyl resonances). The linear dimer (molecule **C**, red circles in Figure 8) could be identified through the strong cross-peaks observed at 44.7 ppm (C_c of molecule **C**): a methyl at 23.5 ppm (C_d of molecule **C**, Scheme 1) in panel IV, an aromatic carbon at 147.7 ppm ($C_{1'}$ of molecule **C**, Scheme 1) and an olefinic carbon at 137.3 ppm (C_b of molecule **C**, Scheme 1) in panel II. The latter carbon could be further connected (panel V) to its neighboring carbon with a chemical shift of 131.1 ppm (C_a of molecule **C**, Scheme 1), whose chemical shift correlates with the ring carbon (C_1 of molecule **C**, Scheme 1) at 139.7 ppm. The formation of 1,3-diphenylbutane ($\mathbf{C_{HT}}$, Scheme 1) from linear dimer (**C**, Scheme 1) is another example of HT-side reaction during styrene dimerization (SI Figure S5).[51]

Interestingly, unlike for the rigid molecules observed in the CP spectra, we do not observe line broadening of the ^{13}C lines of the mobile molecules, as expected due to their mobile nature. However, we do see line-broadening of the proton lines in the J-based (INEPT) $^{13}C-^{1}H$ correlation spectrum (SI Figure S6), which can best be described as a superposition of 2 or more overlapping resonances. This observation explains why our single-molecule fluorescence trajectories behave differently depending on the exact local environment of individual molecules. Additional spin-systems identified in the 2D spectra that could not be assigned to a molecular structure are listed in the Supporting Information (SI Table S2). Herein, the presence of more than four bridging carbon atoms (molecule R1 and M4 in SI Table S2, also Figure 8) are indicative of the formation of trimeric species as was also envisioned by our fluorescence study. Even though these correlations are consistent with the existence of a trimeric product as a result of styrene oligomerization reaction, the absence of additional correlations prohibited us to construct its complete molecular structure. Such partial elucidation (weak/absent NMR signals) could be attributed to its lower quantity and/or overlapping of certain signals.

DFT Calculations: Reversibility of the Proton-Transfer Processes. On the basis of our experimental results, we hypothesized that the stability of the fluorescent carbocations determines the blinking dynamics. We have conducted DFT calculations in order to support this reasoning. The calculations treated the crystallographic MFI unit cell with periodic boundary conditions, using the BEEF-vdW functional[53] to take into account both ion-pair interactions with acid sites and van der Waals interactions with the framework. We calculated electronic energy differences, assuming that they reflect the same trends as free energies for the rigid, confined species considered in this work. First, we determined if the calculations predict a clear preference for adsorption of linear dimeric species in certain locations. We considered the linear dimer of 4-fluorostyrene adsorbed in the following configurations (Table 1): sinusoidal channel (Sinus), straight channel (Straight), intersection region oriented along straight channel (IntStraight), and intersection region oriented along sinusoidal channel (IntSinus). As it can be seen from the Table 1, 4-fluorostyrene is generally more stable in the intersection region directed along the straight pores of MFI, than in other locations, which is the orientation determined experimen-

Table 1. Relative Chemisorption Energies $\Delta\Delta E_{chem}$ (kJ/mol) Calculated for the 4-Fluorostyrene Linear Dimeric Carbocation (C′ in Scheme 1) in H-ZSM-5[a]

BAS location	T1	T2	T3	T5	T7	T9	T12
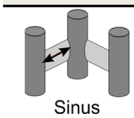 Sinus	100	94	84	90	98	62	70
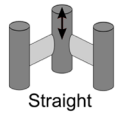 Straight	66	55	57	71	49	80	102
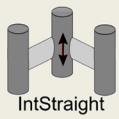 IntStraight	14	17	6	16	24	0	29
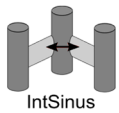 IntSinus	50	70	63	58	67	62	39

[a]T-site numbering of 12 possible crystallographic tetrahedral sites of ZSM-5 follows Kim et al.[54] Numbers are indicated relative to the IntStraight adsorption configuration at the T9 site (ΔE_{chem} = −153 kJ/mol); The IntStraight configuration is highlighted as the most stable. Values can be considered identical if they deviate less than 10 kJ/mol. The adsorption configurations are depicted in the first column. The straight and sinusoidal channels are indicated with dark and light gray, respectively. The black double-arrows indicate the adsorbate position and orientation of its longest axis. For molecules as large as the oligomers considered in this work, there is significant overlap between the locations.

DOI: 10.1021/jacs.8b08041
J. Am. Chem. Soc. 2018, 140, 14195−14205

tally.[40,43] The results indicate that steric interactions outweigh the influence of ion-pair interactions in chemisorption. On the basis of the results from the 4-fluoro species, we calculated chemisorption energies of the 4-methoxy analogue at sites being favorably located for adsorption in the IntStraight configuration (SI Table S3).

We further compared the dimeric species of 4-fluorostyrene and 4-methoxystyrene situated in the intersection region and oriented along the straight channels of the MFI zeolite framework. The calculated protonation energies at individual T sites are indeed consistently smaller for the dimeric species formed from 4-fluorostyrene than those originating from 4-methoxystyrene by about 50 kJ mol^{-1} (Table 2). This agrees with the experimental observation that the dimeric species of 4-methoxystyrene has a higher preference toward the bright carbocationic state than the 4-fluoro analogue does. Note that the calculations aimed at locating the most stable isomers of the carbocations. The neutral dimeric diphenyl alkenes were created as the products from deprotonation of the corresponding fluorescent cations. Hence, the neutral species are not necessarily the most stable isomers, which can explain remarkable photochemistry and stability of the styrene-derived carbocationic species. Whereas the energy of a protonated dimer varies 20 kJ/mol across the investigated acid sites, the energy of the corresponding neutral state varies by 60 kJ/mol. This suggests that the protonation energies are mainly determined by acid-site relaxation and stability of the neutral dimer. As such, we expect proton-transfer-induced blinking behavior to be more pronounced at Brønsted sites that are easily accessible. For example, in the calculations conducted for 4-fluorostyrene, T7 and T8 sites significantly stabilize the neutral dimer of 4-fluorostyrene, relative to the protonated species (Table 2). Hence, these sites are plausible locations of the proton transfer process leading to the blinking fluorescence signal observed experimentally for approximately 50% of the trajectories. In fact, at these acid sites the 4-fluorostyrene-derived dimeric species are equally stable in the neutral and protonated states (within the estimated accuracy of the results). This agrees well with the averaged ratio of $\langle\tau_{on}\rangle/\langle\tau_{off}\rangle \sim 1.2$ (Figure S7), corresponding to free energy differences of 0−5 kJ/mol between the carbocationic and neutral states.

Finally, we have addressed the possibility of formation of the trimeric species. The DFT calculations suggest that it is possible to create trimeric species at the intersections of straight and sinusoidal pores, although the reaction energies generally do not favor trimerization of the 4-fluorostyrene species (SI Table S4). We expect the same to be the case for the 4-methoxystyrene trimers, although in this case the formation is more likely at the crystalline defects.[35]

Table 2. Calculated Energies (kJ/mol) of Protonation of the Para-Substituted Styrene-Derived Dimers at Different Acid Sites within Zeolite H-ZSM-5[a]

R-Sty	T1	T2	T3	T5	T7	T8	T9	T12
4-F	−35	−38	−68	−28	−2	9	−35	−45
4-Meo	−86	−81	−120	−87	−38	−32	−81	−104

[a]All species are situated in the intersection region, oriented along the straight channel.

DISCUSSION

Reaction Mechanism. On the basis of the results described above, we are now in the position to give more general description of the styrene oligomerization reaction mechanism and related blinking dynamics. A reaction pathway for the zeolite (denoted as ZeOH) catalyzed oligomerization of styrene is proposed in Scheme 1. As indicated previously, styrene is first adsorbed on the zeolite and equilibrated between physisorbed (species **A** on non-Brønsted acid site, Scheme 1) and π-complex state (species **A′** on Brønsted acid site, Scheme 1). The reaction is initiated with the subsequent formation of chemisorbed carbenium ion (an ion-pair species **A″**, Scheme 1) and followed by covalently bonded surface-alkoxide (species **B**, Scheme 1). This step is proposed to be the rate-determining step during the zeolite catalyzed dimerization of alkene reaction.[8] The surface-alkoxy species then react with another styrene molecule to form both linear (**C**) and cyclic (**D**) dimers, via linear (**C′**) and cyclic (**D′**) chemisorbed carbenium species, respectively. Two other side products, ethylbenzene ($\mathbf{B_{HT}}$) and 1,3-diphenylbutane ($\mathbf{C_{HT}}$), were formed from chemisorbed **A″** and **C′** carbenium species respectively, as a result of hydrogen-transfer reactions over zeolite.[51] Our fluorescence microscopy blinking observations (Figure 2) and DFT calculations (Table 2) indicate that the single proton transfer/exchange between protonated linear dimeric fluorescent carbocation (**C′**) and nonfluorescent 1,3 diphenyl-1-butene (**C**) can be reversible in nature. Thus, it is safe to assume that dimeric carbocation **C′** simultaneously undergoes through two different chemical transformation: (i) *reversible* single-proton transfer to **C** and (ii) *irreversible* hydrogen transfer to $\mathbf{C_{HT}}$. This phenomenon not only indicates the "site-dependent" claim from the fluorescence intermittency results in the single-molecule fluorescence experiments, but also suggests the hydrogen-transfer pathway as a possible quenching route. Moreover, the simultaneous existence of both linear (**C**) and cyclic (**D**) dimerized products further supports heterogeneities in acid site strengths within a zeolite crystal, as the cyclic product is supposed to form on stronger acid sites and most likely close to crystalline defects.[42,55] Similarly, the observed line-broadening of the proton lines of *syn*-**D** and *anti*-**D** isomers in the INEPT $^{13}C-^{1}H$ correlation spectrum (as illustrated in Figure S6) could be attributed to their presence in the nonidentical zeolite environment. It should be noted that our NMR studies failed to detect 1,3-diphenyl-1,3-butadiene (i.e., the absence of any cross peak between 110 and 115 ppm and 145−150 ppm in the DE based spectra, Figure 7), which inevitably excludes the allylic species as a possible candidate for fluorescent carbocationic species in the present study. This observation is consistent with the recent TD-DFT calculations, where it has been suggested that the linear dimeric carbocations **C′** can absorb light in the visible region.[44]

Site-Dependent Stability and Blinking of the Fluorescent Carbocationic Species. We relate the observed fluorescence blinking behavior of 4-methoxystyrene and 4-fluorostyrene to differences in the proton transfer between linear carbocationic species **C′** (or their trimeric analogues) and the BAS. As shown in our earlier work, zeolite ZSM-5 crystals exposed to 4-fluorostyrene do not show visible reactivity (coloration) in bulk UV−vis experiments at room temperature, whereas 4-methoxystyrene reacts immediately producing blue coloration of the crystals.[40,41] Nevertheless,

DOI: 10.1021/jacs.8b08041
J. Am. Chem. Soc. 2018, 140, 14195−14205

single-molecule fluorescence microscopy can detect extremely low reactivity of 4-fluorostyrene, with 4 orders of magnitude lower turnover rates than of 4-methoxystyrene.[35] This instability of 4-fluorostyrene carbocations explains why fluorescence of these emitters was accompanied with significant blinking, also in line with the DFT calculations. Our fluorescence blinking analysis (Figures 2 and 3) and solid-state NMR spectroscopy (Figure 6) suggests that individual fluorescent molecules may experience different local environments, as reflected in their blinking behavior (or the absence of blinking). This observation also provides indirect justification that side reactions (i.e., cyclization and/or hydrogen-transfer) of fluorescent linear dimeric products occur over zeolite acid sites, as illustrated in Scheme 1.

Several arguments point toward an observation of proton-transfer and/or related hydrogen-transfer processes. First, we experimentally detect distinct subpopulations of carbocations with different fluorescence behavior. As we observe both blinking and nonblinking subpopulations, the results suggest that blinking properties are closely related to chemical stability of fluorescent carbocations at specific crystallographic locations in the framework. Second, fluorescence intermittence patterns alone can be further classified into subgroups of quantitatively similar behavior, according to the duration and frequency of fluorescent and dark states. Another possibility that we considered is hopping of fluorescent species between acid sites and in and out of polarization plane (i.e., between sinusoidal and straight pores). This scenario is difficult to rationalize as we did not observe appreciable fluorescence along sinusoidal pores. In addition, site-hopping would be followed by measurable diffusion (over 10 min interval) and blinking patterns would not have distinct signatures. In contrast, analyzed emitters were static in all cases to the positional accuracy of 20 nm.

It is interesting to compare the equilibrium constant, K, of the reversible protonation reaction, $K = \langle\tau_{on}\rangle/\langle\tau_{off}\rangle$, for both reactants (Figure S7). For 4-fluorostyrene emitters, the median value is at $K = 0.7$, with relatively small dispersion. For 4-methoxystyrene emitters, the values range from $K = 0.3$ (larger dark lifetimes) to $K = 100$ (significantly larger fluorescent times). Nevertheless, the measured equilibrium constants can only account for the free energy differences in the range of ±10 kJ/mol. Whereas these values fit well with the DFT calculations for 4-fluorostyryrene, they are smaller than the calculated values for 4-methoxystyrene (Table 2). In this case, the dimeric carbocationic species were found to be more stable than the neutral dimers at all T-site locations, when the species were situated along straight pores at the intersection region (Table 2); these sites could be the plausible candidates for *nonblinking* trajectories. Keeping in mind that we only considered a small fraction of the large number of proton locations, adsorption configurations and adsorbate isomers, other less-stable sites may be able to induce the blinking behavior of 4-methoxystyrene emitters observed in Figures 2−4.

The behavior of 4-methoxystyrene is more complex to rationalize in terms of fluorescence behavior and dispersion of lifetimes, as this compound is highly reactive and leads to the formation of at least two types of distinguishable fluorescence species.[35] This is in line with many emitters of 4-methoxystyrene observed without blinking, especially on parent zeolite crystals and in highly diluted *n*-heptane solutions. Previously, we reported on reaction conditions that lead to the formation of highly photostable fluorescent species of 4-methoxystyrene.[35] The fluorescent products of this reactant only showed pronounced blinking at the conditions of high acid-site accessibility and presumably formation of trimeric (or other more photostable) fluorescent species. Therefore, it is likely that the trimeric species are also contributing to the highly photostable and blinking trajectories. At present, we can only speculate if the existence of other types of fluorophores may contribute to the observed fluorescence behavior, although the number of candidates is limited due to spatial constrains of ZSM-5. As the length and diversity of trajectories grow with introducing crystalline defects in zeolite framework, we speculate that several distinct nanoenvironments exist around fluorescent carbocationic species. The solid-state NMR studies also indicate simultaneous existence of hydrogen-transfer product of neutral and nonfluorescent 1,3-diphenyl-1-butene and its corresponding carbocation, supporting further the site-heterogeneity of zeolite ZSM-5.

Finally, we show that zeolites can be excellent hosts to stabilize protonated organic intermediates[56,57] and that this chemistry can lead to highly fluorescent carbocationic species protected from the nucleophilic attacks. This suggests that stability of carbocations in zeolites can be significantly different from those in solution, leading to their remarkable fluorescence properties. This especially holds true for thermodynamically more stable 4-methoxystyrene, where we observed fluorescent carbocationic emitters stable for longer than 20 min of constant laser radiation.

CONCLUSION

We have demonstrated a powerful fluorescence microscopy approach to study single-molecule blinking dynamics and stability of individual carbocationic species in the highly confined spaces of a zeolite host. Supported by advanced solid-state NMR spectroscopy and DFT calculations, our results indicate that the relative stability and location of the formed fluorescent carbocationic species determines their blinking behavior and statistical distribution fluorescent and dark states. Depending on the nearest-neighbor molecular environment, fluorescence switching can span large time scales of carbocationic stability and proton-transfer rates. In this respect, the single-site/single-molecule approach clearly shows that the equilibrium between carbocation and neutral states can be significantly shifted by changing substituents and solvents.

Simultaneously, solid-state NMR spectroscopy was utilized for the accurate structural elucidation of the reaction products after the dimerization of styrene reaction over H-ZSM-5. Multiple adsorption modes of olefin (i.e., styrene in the present case) along with both linear and cyclic dimeric products were primarily observed by solid-state NMR spectroscopy. Additionally, the results also identify the mobility-dependent features within the zeolitic framework and an additional hydrogen transfer-based side-reaction route.

Our combined spectroscopic and theory approach collectively advocates the concept of a hybrid inorganic−organic nature of the working catalyst material, constituted by the inorganic zeolite and organic trapped species during a catalytic reaction. The vicinity of the framework Al and the distinctive host−guest chemistry between the zeolite and the trapped hydrocarbons play a governing role in the product formation. In a broader perspective, our findings will not only have important implications for understanding proton/hydrogen transfer processes in zeolites and the formation/behavior of

DOI: 10.1021/jacs.8b08041
J. Am. Chem. Soc. 2018, 140, 14195−14205

highly photostable emitters confined in microporous hosts, but will also contribute to the basic understanding of zeolite-catalyzed hydrocarbon conversion chemistry.

■ ASSOCIATED CONTENT

Supporting Information

The Supporting Information is available free of charge on the ACS Publications website at DOI: 10.1021/jacs.8b08041.

Supporting figures and tables, single molecule fluorescence trajectories, NMR data, and DFT calculations (PDF)

Movie S1 (AVI)

Movie S2 (AVI)

■ AUTHOR INFORMATION

Corresponding Author

*b.m.weckhuysen@uu.nl

ORCID

Abhishek Dutta Chowdhury: 0000-0002-4121-7375

Johan Hofkens: 0000-0002-9101-0567

Bert M. Weckhuysen: 0000-0001-5245-1426

Notes

The authors declare no competing financial interest.

■ ACKNOWLEDGMENTS

B.M.W. acknowledges The Netherlands Organization for Scientific Research (NWO) for a Gravitation program (Netherlands Center for Multiscale Catalytic Energy Conversion, MCEC) and a European Research Council (ERC) Advanced Grant (321140). This project has also received funding from the European Union's Horizon 2020 research and innovation program under the Marie Skłodowska-Curie grant agreement (no. 704544 to A.D.C.), a Middelgroot program (no. 700.58.102 to M.B.), and uNMR-NL, an NWO-funded National Roadmap Large-Scale Facility for The Netherlands (no. 184.032.207). R.Y.B acknowledges The Norwegian High Performance Computing program for resources at the Abel cluster under project no. nn4683k, and the USIT center at University of Oslo for support.

■ REFERENCES

(1) Ertl, G., Knozinger, H., Weitkamp, J., Eds.; *Handbook of Heterogeneous Catalysis*; Wiley-VCH: Weinheim, 2008.

(2) Hagen, J. *Industrial Catalysis: A Practical Approach*; Wiley-VCH: Weinheim, 2005.

(3) Čejka, J., Corma, A., Zones, S., Eds.; *Zeolites and Catalysis: Synthesis, Reactions and Applications*; Wiley-VCH: Weinheim, 2010.

(4) Corma, A. Application of Zeolites in Fluid Catalytic Cracking and Related Processes. *Stud. Surf. Sci. Catal.* **1989**, *49*, 49−67.

(5) Stöcker, M. Methanol to Olefins (MTO) and Methanol to Gasoline (MTG). In *Zeolites and Catalysis: Synthesis, Reactions and Applications*; Čejka, J., Corma, A., Zones, S., Eds.; Wiley-VCH: Weinheim, 2010; pp 687−711.

(6) Kramer, G. J.; Van Santen, R. A. Theoretical Determination of Proton Affinity Differences in Zeolites. *J. Am. Chem. Soc.* **1993**, *115* (7), 2887−2897.

(7) Hunger, M. Catalytically Active Sites: Generation and Characterization. In *Zeolites and Catalysis: Synthesis, Reactions and Applications*; Čejka, J., Corma, A., Zones, S., Eds.; Wiley-VCH: Weinheim, 2010; pp 493−546.

(8) Schallmoser, S.; Haller, G. L.; Sanchez-Sanchez, M.; Lercher, J. A. Role of Spatial Constraints of Brønsted Acid Sites for Adsorption and Surface Reactions of Linear Pentenes. *J. Am. Chem. Soc.* **2017**, *139* (25), 8646−8652.

(9) Ehresmann, J. O.; Wang, W.; Herreros, B.; Luigi, D.-P.; Venkatraman, T. N.; Song, W.; Nicholas, J. B.; Haw, J. F. Theoretical and Experimental Investigation of the Effect of Proton Transfer on the 27Al MAS NMR Line Shapes of Zeolite−Adsorbate Complexes: An Independent Measure of Solid Acid Strength. *J. Am. Chem. Soc.* **2002**, *124* (36), 10868−10874.

(10) Han, O. H.; Kim, C.-S.; Hong, S. B. Direct Evidence for the Nonrandom Nature of Al Substitution in Zeolite ZSM-5: An Investigation by ^{27}Al MAS and MQ MAS NMR. *Angew. Chem., Int. Ed.* **2002**, *41* (3), 469−472.

(11) Stavitski, E.; Weckhuysen, B. M. Vibrational Spectroscopy and Related In Situ Studies of Catalytic Reactions within Molecular Sieves. In *Zeolites and Catalysis: Synthesis, Reactions and Applications*; Čejka, J., Corma, A., Zones, S., Eds.; Wiley-VCH: Weinheim, 2010; pp 209−236.

(12) Bordiga, S.; Lamberti, C.; Bonino, F.; Travert, A.; Thibault-Starzyk, F. Probing Zeolites by Vibrational Spectroscopies. *Chem. Soc. Rev.* **2015**, *44* (20), 7262−7341.

(13) Vjunov, A.; Fulton, J. L.; Huthwelker, T.; Pin, S.; Mei, D.; Schenter, G. K.; Govind, N.; Camaioni, D. M.; Hu, J. Z.; Lercher, J. A. Quantitatively Probing the Al Distribution in Zeolites. *J. Am. Chem. Soc.* **2014**, *136* (23), 8296−8306.

(14) van Bokhoven, J. A.; van der Eerden, A. M. J.; Koningsberger, D. C. Three-Coordinate Aluminum in Zeolites Observed with In Situ X-Ray Absorption Near-Edge Spectroscopy at the Al K-Edge: Flexibility of Aluminum Coordinations in Zeolites. *J. Am. Chem. Soc.* **2003**, *125* (24), 7435−7442.

(15) Perea, D. E.; Arslan, I.; Liu, J.; Ristanović, Z.; Kovarik, L.; Arey, B. W.; Lercher, J. A.; Bare, S. R.; Weckhuysen, B. M. Determining the Location and Nearest Neighbours of Aluminium in Zeolites with Atom Probe Tomography. *Nat. Commun.* **2015**, *6*, 7589.

(16) Schmidt, J. E.; Oord, R.; Guo, W.; Poplawsky, J. D.; Weckhuysen, B. M. Nanoscale Tomography Reveals the Deactivation of Automotive Copper-Exchanged Zeolite Catalysts. *Nat. Commun.* **2017**, *8*, 1666.

(17) Cremer, G. D.; Sels, B. F.; De Vos, D. E.; Hofkens, J.; Roeffaers, M. B. J. Fluorescence Micro(Spectro)Scopy as a Tool to Study Catalytic Materials in Action. *Chem. Soc. Rev.* **2010**, *39* (12), 4703−4717.

(18) Chen, P.; Zhou, X.; Shen, H.; Andoy, N. M.; Choudhary, E.; Han, K.-S.; Liu, G.; Meng, W. Single-Molecule Fluorescence Imaging of Nanocatalytic Processes. *Chem. Soc. Rev.* **2010**, *39* (12), 4560−4570.

(19) Cordes, T.; Blum, S. A. Opportunities and Challenges in Single-Molecule and Single-Particle Fluorescence Microscopy for Mechanistic Studies of Chemical Reactions. *Nat. Chem.* **2013**, *5* (12), 993−999.

(20) Chen, T.; Dong, B.; Chen, K.; Zhao, F.; Cheng, X.; Ma, C.; Lee, S.; Zhang, P.; Kang, S. H.; Ha, J. W.; Xu, W.; Fang, N. Optical Super-Resolution Imaging of Surface Reactions. *Chem. Rev.* **2017**, *117* (11), 7510−7537.

(21) Roeffaers, M. B. J.; Sels, B. F.; Uji-i, H.; De Schryver, F. C.; Jacobs, P. A.; De Vos, D. E.; Hofkens, J. Spatially Resolved Observation of Crystal-Face-Dependent Catalysis by Single Turnover Counting. *Nature* **2006**, *439* (7076), 572−575.

(22) Xu, W.; Kong, J. S.; Yeh, Y.-T. E.; Chen, P. Single-Molecule Nanocatalysis Reveals Heterogeneous Reaction Pathways and Catalytic Dynamics. *Nat. Mater.* **2008**, *7* (12), 992−996.

(23) Tachikawa, T.; Majima, T. Exploring the Spatial Distribution and Transport Behavior of Charge Carriers in a Single Titania Nanowire. *J. Am. Chem. Soc.* **2009**, *131* (24), 8485−8495.

(24) Hensle, E. M.; Blum, S. A. Phase Separation Polymerization of Dicyclopentadiene Characterized by In Operando Fluorescence Microscopy. *J. Am. Chem. Soc.* **2013**, *135* (33), 12324−12328.

(25) Sambur, J. B.; Chen, T.-Y.; Choudhary, E.; Chen, G.; Nissen, E. J.; Thomas, E. M.; Zou, N.; Chen, P. Sub-Particle Reaction and

Photocurrent Mapping to Optimize Catalyst-Modified Photoanodes. *Nature* **2016**, *530* (7588), 77−80.
(26) Zürner, A.; Kirstein, J.; Döblinger, M.; Bräuchle, C.; Bein, T. Visualizing Single-Molecule Diffusion in Mesoporous Materials. *Nature* **2007**, *450* (7170), 705−708.
(27) De Cremer, G.; Roeffaers, M. B. J.; Bartholomeeusen, E.; Lin, K.; Dedecker, P.; Pescarmona, P. P.; Jacobs, P. A.; De Vos, D. E.; Hofkens, J.; Sels, B. F. High-Resolution Single-Turnover Mapping Reveals Intraparticle Diffusion Limitation in Ti-MCM-41-Catalyzed Epoxidation. *Angew. Chem., Int. Ed.* **2010**, *49* (5), 908−911.
(28) Hendriks, F. C.; Meirer, F.; Kubarev, A. V.; Ristanović, Z.; Roeffaers, M. B. J.; Vogt, E. T. C.; Bruijnincx, P. C. A.; Weckhuysen, B. M. Single-Molecule Fluorescence Microscopy Reveals Local Diffusion Coefficients in the Pore Network of an Individual Catalyst Particle. *J. Am. Chem. Soc.* **2017**, *139* (39), 13632−13635.
(29) Zou, N.; Zhou, X.; Chen, G.; Andoy, N. M.; Jung, W.; Liu, G.; Chen, P. Cooperative Communication within and between Single Nanocatalysts. *Nat. Chem.* **2018**, *1*, 607.
(30) Roeffaers, M. B. J.; De Cremer, G.; Libeert, J.; Ameloot, R.; Dedecker, P.; Bons, A.-J.; Bückins, M.; Martens, J. A.; Sels, B. F.; De Vos, D. E.; Hofkens, J. Super-Resolution Reactivity Mapping of Nanostructured Catalyst Particles. *Angew. Chem., Int. Ed.* **2009**, *48* (49), 9285−9289.
(31) Ristanović, Z.; Kerssens, M. M.; Kubarev, A. V.; Hendriks, F. C.; Dedecker, P.; Hofkens, J.; Roeffaers, M. B. J.; Weckhuysen, B. M. High-Resolution Single-Molecule Fluorescence Imaging of Zeolite Aggregates within Real-Life Fluid Catalytic Cracking Particles. *Angew. Chem., Int. Ed.* **2015**, *54* (6), 1836−1840.
(32) Liu, K.-L.; Kubarev, A. V.; Van Loon, J.; Uji-i, H.; De Vos, D. E.; Hofkens, J.; Roeffaers, M. B. J. Rationalizing Inter- and Intracrystal Heterogeneities in Dealuminated Acid Mordenite Zeolites by Stimulated Raman Scattering Microscopy Correlated with Super-Resolution Fluorescence Microscopy. *ACS Nano* **2014**, *8* (12), 12650−12659.
(33) Ristanović, Z.; Hofmann, J. P.; De Cremer, G.; Kubarev, A. V.; Rohnke, M.; Meirer, F.; Hofkens, J.; Roeffaers, M. B. J.; Weckhuysen, B. M. Quantitative 3D Fluorescence Imaging of Single Catalytic Turnovers Reveals Spatiotemporal Gradients in Reactivity of Zeolite H-ZSM-5 Crystals upon Steaming. *J. Am. Chem. Soc.* **2015**, *137* (20), 6559−6568.
(34) Kubarev, A. V.; Janssen, K. P. F.; Roeffaers, M. B. J. Noninvasive Nanoscopy Uncovers the Impact of the Hierarchical Porous Structure on the Catalytic Activity of Single Dealuminated Mordenite Crystals. *ChemCatChem* **2015**, *7* (22), 3646−3650.
(35) Ristanović, Z.; Kubarev, A. V.; Hofkens, J.; Roeffaers, M. B. J.; Weckhuysen, B. M. Single Molecule Nanospectroscopy Visualizes Proton-Transfer Processes within a Zeolite Crystal. *J. Am. Chem. Soc.* **2016**, *138* (41), 13586−13596.
(36) Kubarev, A. V.; Breynaert, E.; Van Loon, J.; Layek, A.; Fleury, G.; Radhakrishnan, S.; Martens, J.; Roeffaers, M. B. J. Solvent Polarity-Induced Pore Selectivity in H-ZSM-5 Catalysis. *ACS Catal.* **2017**, *7* (7), 4248−4252.
(37) Van Loon, J.; Janssen, K. P. F.; Franklin, T.; Kubarev, A. V.; Steele, J. A.; Debroye, E.; Breynaert, E.; Martens, J. A.; Roeffaers, M. B. J. Rationalizing Acid Zeolite Performance on the Nanoscale by Correlative Fluorescence and Electron Microscopy. *ACS Catal.* **2017**, *7* (8), 5234−5242.
(38) Lu, H. P.; Xun, L.; Xie, X. S. Single-Molecule Enzymatic Dynamics. *Science* **1998**, *282* (5395), 1877−1882.
(39) Fornés, V.; García, H.; Martí, V.; Fernández, L. Carbenium Ions Generated upon Adsorption of 4-Methoxystyrenes onto Acid Zeolites. A Kinetic Study. *Tetrahedron* **1998**, *54* (15), 3827−3832.
(40) Kox, M. H. F.; Stavitski, E.; Weckhuysen, B. M. Nonuniform Catalytic Behavior of Zeolite Crystals as Revealed by In Situ Optical Microspectroscopy. *Angew. Chem., Int. Ed.* **2007**, *46* (20), 3652−3655.
(41) Stavitski, E.; Kox, M. H. F.; Weckhuysen, B. M. Revealing Shape Selectivity and Catalytic Activity Trends Within the Pores of H-ZSM-5 Crystals by Time- and Space-Resolved Optical and Fluorescence Microspectroscopy. *Chem. - Eur. J.* **2007**, *13* (25), 7057−7065.
(42) Buurmans, I. L. C.; Pidko, E. A.; Groot, J. M. de; Stavitski, E.; Santen, R. A. v.; Weckhuysen, B. M. Styrene Oligomerization as a Molecular Probe Reaction for Zeolite Acidity: A UV-Vis Spectroscopy and DFT Study. *Phys. Chem. Chem. Phys.* **2010**, *12* (26), 7032−7040.
(43) Sprung, C.; Weckhuysen, B. M. Differences in the Location of Guest Molecules within Zeolite Pores As Revealed by Multilaser Excitation Confocal Fluorescence Microscopy: Which Molecule Is Where? *J. Am. Chem. Soc.* **2015**, *137* (5), 1916−1928.
(44) Valencia, D. Elucidating the Structure of Light Absorbing Styrene Carbocation Species Formed within Zeolites. *Phys. Chem. Chem. Phys.* **2017**, *19* (23), 15050−15058.
(45) Andronesi, O. C.; Becker, S.; Seidel, K.; Heise, H.; Young, H. S.; Baldus, M. Determination of Membrane Protein Structure and Dynamics by Magic-Angle-Spinning Solid-State NMR Spectroscopy. *J. Am. Chem. Soc.* **2005**, *127*, 12965−12974.
(46) Labokha, A. A.; Gradmann, S.; Frey, S.; Hülsmann, B. B.; Urlaub, H.; Baldus, M.; Görlich, D. Systematic Analysis of Barrier-Forming FG Hydrogels from Xenopus Nuclear Pore Complexes. *EMBO J.* **2013**, *32* (4), 204−218.
(47) Chowdhury, A. D.; Houben, K.; Whiting, G. T.; Mokhtar, M.; Asiri, A. M.; Al-Thabaiti, S. A.; Baldus, M.; Weckhuysen, B. M. Initial Carbon−carbon Bond Formation during the Early Stages of the Methanol-to-Olefin Process Proven by Zeolite-Trapped Acetate and Methyl Acetate. *Angew. Chem., Int. Ed.* **2016**, *55*, 15840−15845.
(48) Chowdhury, A. D.; Houben, K.; Whiting, G. T.; Chung, S.-H.; Baldus, M.; Weckhuysen, B. M. Electrophilic Aromatic Substitution over Zeolites Generates Wheland-Type Reaction Intermediates. *Nat. Catal.* **2018**, *1*, 23−31.
(49) Morris, G. A.; Freeman, R. Enhancement of Nuclear Magnetic Resonance Signals by Polarization Transfer. *J. Am. Chem. Soc.* **1979**, *101* (3), 760−762.
(50) Pines, A.; Gibby, M. G.; Waugh, J. S. Proton-Enhanced NMR of Dilute Spins in Solids. *J. Chem. Phys.* **1973**, *59* (2), 569−590.
(51) Müller, S.; Liu, Y.; Kirchberger, F. M.; Tonigold, M.; Sanchez-Sanchez, M.; Lercher, J. A. Hydrogen Transfer Pathways during Zeolite Catalyzed Methanol Conversion to Hydrocarbons. *J. Am. Chem. Soc.* **2016**, *138* (49), 15994−16003.
(52) Weingarth, M.; Demco, D. E.; Bodenhausen, G.; Tekely, P. Improved Magnetization Transfer in Solid-State NMR with Fast Magic Angle Spinning. *Chem. Phys. Lett.* **2009**, *469*, 342−348.
(53) Wellendorff, J.; Lundgaard, K. T.; Møgelhøj, A.; Petzold, V.; Landis, D. D.; Nørskov, J. K.; Bligaard, T.; Jacobsen, K. W. Density Functionals for Surface Science: Exchange-Correlation Model Development with Bayesian Error Estimation. *Phys. Rev. B: Condens. Matter Mater. Phys.* **2012**, *85* (23), 235149.
(54) Kim, C. W.; Heo, N. H.; Seff, K. Framework Sites Preferred by Aluminum in Zeolite ZSM-5. Structure of a Fully Dehydrated, Fully Cs^+-Exchanged ZSM-5 Crystal (MFI, Si/Al = 24). *J. Phys. Chem. C* **2011**, *115* (50), 24823−24838.
(55) Benito, A.; Corma, A.; García, H.; Primo, J. Dimerization of Styrene Catalyzed by Acid 12-Membered Ring Zeolites. *Appl. Catal., A* **1994**, *116* (1−2), 127−135.
(56) Bjørgen, M.; Bonino, F.; Kolboe, S.; Lillerud, K.-P.; Zecchina, A.; Bordiga, S. Spectroscopic Evidence for a Persistent Benzenium Cation in Zeolite H-Beta. *J. Am. Chem. Soc.* **2003**, *125* (51), 15863−15868.
(57) Bjørgen, M.; Bonino, F.; Arstad, B.; Kolboe, S.; Lillerud, K.-P.; Zecchina, A.; Bordiga, S. Persistent Methylbenzenium Ions in Protonated Zeolites: The Required Proton Affinity of the Guest Hydrocarbon. *ChemPhysChem* **2005**, *6* (2), 232−235.

DOI: 10.1021/jacs.8b08041
J. Am. Chem. Soc. 2018, 140, 14195−14205